High-resolution wind risk mapping of structures deployed along line-like infrastructures: General framework and application

Original
High-resolution wind risk mapping of structures deployed along line-like infrastructures: General framework and application / Raffaele, Lorenzo. - In: ENGINEERING STRUCTURES. - ISSN 0141-0296. - 359:(2026). [10.1016/j.engstruct.2026.122756]

Publisher:
Elsevier

Published
DOI:10.1016/j.engstruct.2026.122756

Engineering Structures 359 (2026) 122756

Contents lists available at ScienceDirect

Engineering Structures

journal homepage: www.elsevier.com/locate/engstruct

High-resolution wind risk mapping of structures deployed along line-like infrastructures: General framework and application

Lorenzo Raffaele

GeoWindy R&D Group, Department of Architecture and Design, Politecnico di Torino, Viale Mattioli 39, Torino, 10126, Italy

ARTICLE INFO

Keywords:
Wind hazard
Vulnerability
Exposure
Wind risk
Mapping
Line-like infrastructure
Lattice tower

ABSTRACT

The lack of high-resolution wind hazard maps has long limited the development of comprehensive wind risk assessments for countrywide infrastructures. This study introduces an integrated probabilistic framework for evaluating and mapping the wind failure risk of point-like structural assets deployed along line-like infrastructure systems. The feasibility of the approach is demonstrated by focusing on a particular infrastructure class, i.e. lattice towers along overhead power lines, with a specific application to a transnational transmission corridor between Italy and Switzerland. The wind hazard model is grounded on a novel high-resolution omnidirectional wind speed mesoscale mapping methodology taking advantage of downscaled reanalysis dataset. Structural vulnerability is characterized through literature-based fragility curves for lattice towers. Exposure is defined through geospatial datasets of the Italian and Swiss power networks. The proposed framework enables quantitative estimation of failure probabilities for both individual structures and entire transmission lines, supporting risk-informed design, mitigation, maintenance prioritization, and potential relocation of critical infrastructures. Results are presented through risk maps differing in dimensionality, extent of the covered domain and design perspectives. Transnational 2D risk mapping assists the planning of entire networks. 1D risk mapping supports the design and/or relocation of entire lines. 0D risk mapping supports the design and/or performance assessment of individual lattice towers.

1. Introduction

Wide line-like critical infrastructures include along them multiple recurrent structures, e.g. lattice towers along power lines, bridges along railways, traffic panels along highways, exposed to wind action varying over space and time. The wind risk assessment implicitly requires its countrywide, high-resolution mapping (e.g. [1,2]). In general terms, risk represents the likelihood of failure, i.e. the probability that the demand exerted by actions will exceed the capacity of the structure/infrastructure system to withstand them. Wind-induced risk is characterized by the convolution of the random variables defining wind hazard and structure vulnerability multiplied by the asset exposure, following the so-called Performance-Based Wind Engineering (PBWE) chain [3], originally stemmed from seismic engineering [4].

Wind load is commonly characterized starting from the estimation of the design wind speed, a key point of the “Alan G. Davenport Wind Loading Chain” that continues to guide contemporary Wind Engineering practice (e.g. [5,6]). Traditionally, this estimation relies on a two-step procedure across different spatial scales. In the first step, extreme synoptic wind conditions are mapped at the macroscale (covering areas of several hundred kilometres) through extreme value statistical analyses applied to long-term records from ground-based anemometric stations. This process requires careful collection, correction, and transformation of wind data, followed by their statistical treatment. For an application to the Italian context, see the climatic map drawn by Ballio et al. [7], recently updated by Ricciardelli et al. [8]. The outcome is a set of countrywide climatic wind maps, which then serve as inputs for engineering codes and regulations (e.g. [9,10] in Italy). The second step, referred to as the return criterion [7], is performed by the structural designer. Here, the mapped reference wind speed is translated into a design wind speed that accounts for the specific local characteristics of the site and the project. Adjustments consider factors such as elevation, terrain roughness, topographic effects, proximity to coastal areas, and the chosen reference height above ground. Such a “map-and-return” approach was originally intended to provide site-specific design values for individual projects within a Load-and-Resistance-Factor Design (LRFD, [4]) framework, not to deliver spatially continuous representations of wind hazard expressed through its intensity measure im for given values of the return period T_R. Furthermore, both stages of this methodology present known limitations (see Raffaele et al. [11], for a comprehensive critical discussion).

E-mail address: lorenzo.raffaele@polito.it.

https://doi.org/10.1016/j.engstruct.2026.122756
Received 5 December 2025; Received in revised form 5 March 2026; Accepted 7 April 2026

Among them, the mapping stage is affected by the density and distribution of measurement stations, the duration of available wind records, local installation conditions, and the precision of the instrumentation. The return stage inherits these uncertainties, further complicating the task of quantifying site-dependent effects on the local wind speed. Critical challenges include the subjective evaluation of aerodynamic roughness length z_0, inconsistencies in terrain categorization across standards, and the difficulty of quantifying local orographic effects.

Structures vulnerability is commonly quantified through fragility curves, which represent the probability that an exposed structure will reach or exceed a specified performance threshold given a certain value of the hazard im. Fragility analysis has a wide background in the seismic engineering field (e.g. [12]), while it has been later transferred within the wind engineering field (e.g. [13]).

The lack of high-resolution wind hazard maps, comparable in resolution and extension to those available for seismic hazard (e.g. [14] for Italy), together with limited implementation of a performance-based engineering framework in wind engineering (e.g. [15]), has so far hindered the drafting of comprehensive wind risk maps. Consequently, unlike the well-established seismic risk mapping (e.g. [16,17] for Italy), the spatial distribution of wind-induced risk remains largely unexplored and poorly quantified over broad areas. This gap represents a critical limitation for the implementation of the PBWE chain for the risk assessment, risk-informed design, as well as for the prioritization of mitigation strategies at regional, national or transnational scales, of wide critical infrastructures.

In the last few years, significant progress has been made in wind risk assessment and mapping along critical infrastructure systems. Despite these advances, a comprehensive, high-resolution risk mapping framework grounded on historically representative long-term data has yet to be established. Hallowell et al. [18] mapped the risk of failure of offshore wind turbines subjected to hurricane-induced wind and wave loads along the US Atlantic coast. Cai et al. [19] quantified the risk of failure of lattice towers along a 31 km-long transmission line in Zhanjiang City exposed to Typhoon Mujigea using a semi-empirical tropical cyclone model. Similarly, Xue et al. [20] assessed the probability of line outages in a benchmark synthetic transmission network affected by Hurricane Harvey, while Ma et al. [21] analysed the outage probability of the power network serving the Lehigh Valley (US) under a time-varying hurricane wind scenario. More recently, Greco et al. [22] proposed a framework for evaluating power line outage probability based on a regional wind model characterized through Weibull probability density functions describing typical wind speeds. Past studies generally (i) evaluate risk under specific or idealized wind scenarios [19–21], (ii) rely on long-term synthetic data generated from parametric hurricane wind models [18], or (iii) base their analyses on parent wind speed distributions rather than on extreme value distributions, more suitable for hazard characterization [22].

Recently, Raffaele et al. [11] introduced a novel high-resolution omnidirectional wind speed mapping methodology that overcomes the inherent limitations of the traditional *map-and-return* approach. The proposed REA-ha framework enables the generation of spatially continuous, implicitly z_0-consistent wind speed maps over wide areas by taking advantage of a first climate REAnalysis step, blending observations with a numerical weather prediction model to derive wind speed across a dense grid [23]. A subsequent height adjustment step allows the estimation of site-specific design wind speeds as a function of the design height. The resulting high-resolution, gap-free wind speed maps provide a robust foundation for a paradigm shift from LRFD to PBWE, thereby bridging the existing gap between wind and seismic risk mappings.

Building on the above considerations, this study aims to address three key research questions: (i) Can the REA-ha approach be leveraged to enhance the definition of the hazard link within the wind risk chain? (ii) Can it be implemented within a comprehensive probabilistic modelling framework to support performance-based design and risk-informed decision-making processes? (iii) If so, which other links in the wind risk chain appear to be comparatively weaker? To address these questions, the study introduces an integrated probabilistic framework for evaluating and mapping the risk of failure of point-like structural assets deployed along line-like infrastructures systems. Lattice towers along overhead power lines are chosen as specific infrastructure class, due to: (i) the extensive national coverage and critical nature of overhead power networks; (ii) their well-documented vulnerability to wind loading (e.g. [24]); and (iii) the high degree of standardization in their structural configurations along transmission corridors [25]. In particular, the proposed framework is applied on a transnational transmission corridor between Italy and Switzerland, selected as a representative and particularly challenging benchmark because of the crossed mountainous geomorphological features, characterized by strong variability in surface roughness and topography.

The paper is organized into four further sections. Section 2 introduces the risk modelling framework and specifies the modelling of each risk determinant, i.e. hazard, vulnerability and exposure. Section 3 discusses the risk determinants by focusing on the specific application of the study. The obtained results are critically discussed in Section 4 by providing risk mappings addressed to different design perspectives. Finally, conclusions of the study are outlined in Section 5.

2. Modelling framework

In this section, the proposed methodological framework for risk assessment of point-like structural assets deployed along line-like infrastructures is presented. This general framework is applicable to a wide range of line-like infrastructure systems. Notable examples include wind risk of lattice towers along power transmission lines (e.g. [19]) and communication networks (e.g. [26]), long-span suspension bridges within national highway networks (e.g. [27]), and traffic signal structures installed along roadways (e.g. [28]). The same framework also encompasses other wind-related hazards, such as ice accretion induced risk on overhead transmission lines (e.g. [29,30]), windblown sand induced risk on point-like technical components (e.g. [31]), tree-fall risk (e.g. [32]), and train-overturning risk (e.g. [33]) along railway lines.

Risk depends on wind hazard, on the vulnerability of the considered assets, and on their exposure, through the chain shown in Fig. 1. The expected annual rate of failure λ_f at coordinates (x, y) is defined through the convolution

$$\lambda_f(x, y) = \int_0^\infty r_U(x, y, u) P_F(x, y, u)\, du \cdot E(x, y), \tag{1}$$

being $r_U(x, y, u)$ the rate of wind extreme events of intensity u at coordinates (x, y), $P_F(x, y, u)$ the asset fragility curve, and $E(x, y)$ the exposure index of the asset. In particular, r_U can be defined from the well known hazard curve $\Lambda(u)$ (in analogy to seismic risk assessment, e.g. [34]), resulting from the annual rate of extreme events $\lambda_{U>u_t}$ together with the conditional Probability Density Function (PDF) of the extreme wind magnitudes $f_{U|U>u_t}$

$$r_U = -\frac{d\Lambda(u)}{du} = \lambda_{U>u_t}(x, y) f_{U|U>u_t}(x, y, u). \tag{2}$$

Then, the probability of failure of the asset P_f results from λ_f by assuming a Poisson process (e.g. [35]):

$$P_f(x, y) = 1 - e^{-\lambda_f}. \tag{3}$$

In this study, the probability of failure of the whole line-like infrastructure $P_{f,line}$ is evaluated starting from the probability of failure of the point-like assets P_f. The correct estimation of $P_{f,line}$ should imply the modelling of interdependencies among consecutive connected assets in terms of both vulnerability (i.e. P_F) and hazard (i.e. r_U). On the one hand, the assessment of the asset fragility curve P_F should be derived from an appropriate model that represents an array of

Fig. 1. Wind risk chain: convolution product (⊛) between mapped hazard and fragility curves multiplied (∗) with mapped exposure.

structures interconnected by the infrastructure (see e.g. [36] for wind vulnerability of overhead power lines). On the other hand, wind hazard scenarios should be statistically defined based on the spatial and temporal scales associated to extreme events occurring along the line-like infrastructure. In other words, wind hazard should account for the proper modelling of the along-line correlation of im (see e.g. [37] for seismic risk along critical infrastructures). It is worth emphasizing that, although several studies on the topic consider the effect of multiple connected structures on vulnerability (e.g. arrays of lattice towers interconnected by conductors in [19]), only a few have considered the spatial correlation of wind intensity measures, either adopting a single wind scenario (e.g. [21]) or through parametric wind models (e.g. [18]). To the Author's best knowledge, to date, however, no study has accounted for the full spatial correlation observed in past wind events. In this study, the line probability of failure is considered bounded in-between the lower bound $\check{P}_{f,line}$, i.e. fully uncorrelated wind hazard along the line giving rise to fully independent failure of the point-like structures, and the upper bound $\hat{P}_{f,line}$, i.e. fully correlated wind hazard along the line giving rise to fully dependent failure of the point-like structures, in agreement with Cai et al. [19]:

$$\begin{aligned} \check{P}_{f,line} &= \max_i \left[P_{f,i}\right] \\ \hat{P}_{f,line} &= 1 - \prod_i \left[1 - P_{f,i}\right]. \end{aligned} \tag{4}$$

where $P_{f,i}$ is the failure probability of the ith tower along the considered line.

In the following subsection, each of the risk determinants illustrated in Fig. 1 is discussed and formally defined, with particular reference to lattice towers deployed along overhead power lines.

2.1. Wind hazard

The adopted wind hazard model is grounded on the REA-ha framework proposed in Raffaele et al. [11]. Such an approach leverages advanced climate reanalyses combining global climate prediction models with satellite observations, their downscaling through regional climate models, and extreme value analysis to finally gather extreme wind speeds. The result is a set of extreme wind speed maps at a 10-metre reference height, provided for multiple return periods T_R. While REA-ha provides discrete return-period wind maps within a LRFD framework, the present study extends the methodology within a PBWE perspective by deriving full spatially continuous hazard curves $\Lambda(x,y,u)$, thus enabling convolution with structural fragility.

Since the introduction of the first global reanalysis dataset in 1997 (ERA-15) to the more recent release in 2023 (ERA5 [38]), ECMWF reanalysis have undergone significant refinements. Their horizontal resolution has improved from about 187 km to roughly 31 km, covering the full spectrum of meso-β atmospheric scales [39]. Temporal sampling has likewise advanced, moving from 6-hourly outputs to hourly data. At the same time, the length of the available records has expanded from 14 years to 83 years. Moreover, in the last years, a variety of strategies for downscaling global reanalysis to regional domains have been explored, though their application in structural engineering, especially for critical infrastructure, remains limited (e.g. [40]). In particular, the Very High Resolution (VHR) dataset developed by CMCC [23] results from the dynamical downscaling of ERA5 to the so-called convection-permitting scale [23], over a domain encompassing Italy and Switzerland (longitude 5°–20°E, latitude 36°–48°N) with a grid spacing of 0.02°, i.e. about 2.2 km, equivalent to the one adopted for the seismic hazard model in Italy [14]. Convection-permitting regional climate models are increasingly gaining attention in the literature, as they (i) enhance accuracy and sensitivity to climate change [41], (ii) enable an accurate depiction of the effects of heterogeneous surface roughness and complex orography on the design wind speed [11], and (iii) achieve high spatial resolution up to the so-called meso-γ atmospheric scale.

In the light of the above, the REA-ha approach introduces several methodological advantages. In particular, (i) reanalysis wind speed data is homogeneously sampled in space and time and it is intrinsically self consistent; (ii) mesoscale effects, including orographic and roughness influences, are consistently and explicitly resolved, while microscale effects are purposefully excluded by the analysis; (iii) the fine spatial resolution and continuous temporal sampling of the wind speed yield comprehensive gap-free maps of extreme wind speeds. Nonetheless, REA-based estimates of extreme wind speeds tend to show a negative bias relative to observations, particularly for high T_R [11]. To address this, the proposed methodology incorporates a calibrated correction factor that adjusts the modelled extremes as a function of T_R. Accordingly, im at given coordinates (x,y) can be expressed by the extreme wind speed as:

$$U_{T_R}(x,y) = \gamma_{m,T_R} U_{REA,T_R}(x,y) \tag{5}$$

where U_{REA,T_R} is the mapped wind speed from REA stage defined at the standard reference height $z_{ref} = 10$ m with a return period T_R, and γ_{m,T_R} is a model correction factor.

γ_{m,T_R} compensates REA-based estimations depending on T_R, thereby adjusting the bias of extreme wind speed quantiles. It is derived by comparing extreme wind speeds resulting from REA step and anemometric measurements in correspondence of 10 compliant anemometric stations in terms of wind measurement completeness, steadiness, uniformity of flat orography and roughness. According to Raffaele et al. [11], the model correction factor is obtained as:

$$\gamma_{m,T_R} = \frac{1}{1 + \bar{\varepsilon}_{REA-stat}} \tag{6}$$

being $\bar{\varepsilon}_{REA-stat}$ the average relative error between Reanalysis and measurements in correspondence of compliant stations.

U_{REA,T_R} is assessed by adopting Peaks Over Threshold (POT) approach (e.g. [42]). The threshold u_t of each time series is set equal to the lowest annual maxima detected along the same time series [43]. Then, independence of extreme events is ensured by filtering extremes from consecutive events occurring within two days. In such a way, the exceedances constitute an independent identically distributed sample. Finally, exceedances over u_t are fitted with Generalized Pareto Distributions (GPD) $f_{U|U>u_t}$. According to Coles [44], the T_R-year return speed U_{REA,T_R} can be then obtained as:

$$U_{REA,T_R}(x,y) = u_t(x,y) + \frac{\sigma_U(x,y)}{k_U(x,y)} \left[\left(\lambda_{U>u_t}(x,y) T_R \right)^{k_U(x,y)} - 1 \right], \tag{7}$$

where u_t is the GPD threshold, σ_U is the GPD scale factor, k_U is the GPD shape factor, and $\lambda_{U>u_t}$ is the average rate of independent exceedances per year.

Fig. 2(a–d) shows a glimpse of the 3D map of the intensity measure U_{T_R} based on the VHR dataset by setting $T_R = \{2, 50, 100, 200\}$ years. The maps result from the statistical processing of approximately 163.5 billion wind speed observations distributed over 4.44e+6 cells, each with a horizontal resolution of about 2.2 km. The high spatial resolution of the maps provides a substantially more detailed depiction of extreme wind speeds compared to the current zoning defined in Italian [9] and Swiss [45] standards. Furthermore, they already embody orography and roughness effects up to the meso-γ scale. The

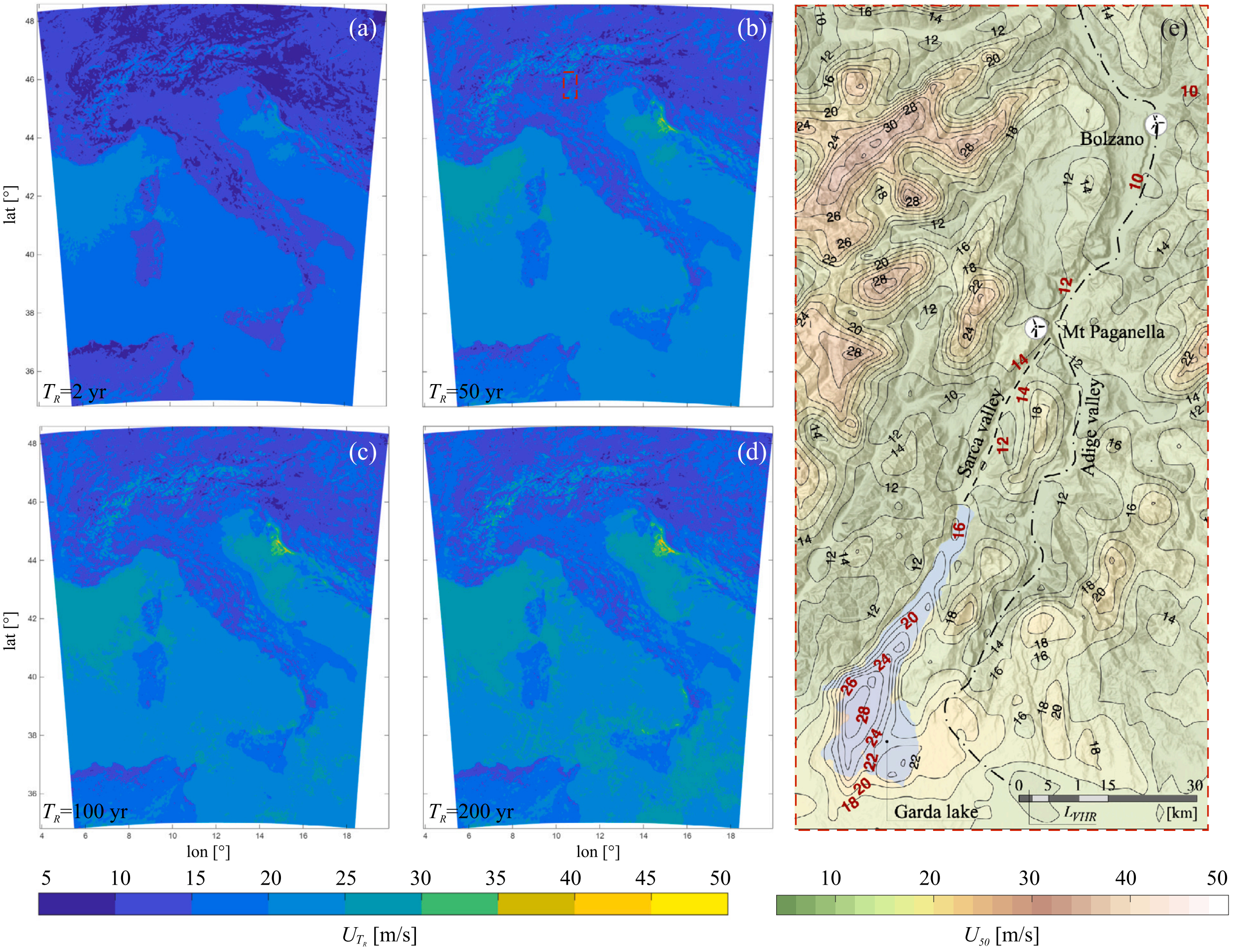

Fig. 2. Hazard maps of extreme wind speed with return period $T_R = 2$ (a), $T_R = 50$ (b), $T_R = 100$ (c), $T_R = 200$ (d) yr. Close-up view around the zone surrounding the Adige and Sarca valleys, from Bolzano to the Garda lake (e) for $T_R = 50$ yr.

largest wind speeds are observed over water bodies (seas and lakes), due to their low z_0, and along mountain ridges, where orographic effects are explicitly incorporated. In absolute terms, the highest wind speeds occur along the Croatian coastline near the Velebit mountain ridge, a region known for intense Bora winds [46]. Particularly strong wind areas include the Strait of Bonifacio, where channelling between northern Sardinia and southern Corsica intensifies wind speed, and the Tyrrhenian coasts of Sicily and Calabria, where complex coastal orography strongly affects local wind patterns.

The effects induced by orography and roughness are exemplified in the close-up view in Fig. 2(e) ranging from Bolzano to Garda lake. U_{50} is lower in proximity of Bolzano, it slightly increases along the Sarca valley due to its narrowing. The microscale features of the wind speed-up at the top of Mt. Paganella are not caught, consistently with the mesoscale resolution of the approach. At the mouth of Sarca valley and over the Garda lake wind speed dramatically increases. Such a mesoscale speed-up is due to (i) the contribution of strong mesoscale Foehn winds blowing from northeast and directed along the major axis of the lake [47], (ii) the surrounding steep orography, and (iii) the low local roughness of the stretch of water.

Beyond the estimation of discrete return levels U_{T_R}, the adopted POT-GPD formulation enables the derivation of a continuous wind hazard model. In this study, exceedances are transformed through the T_R-dependent nonlinear mapping defined in Eq. (5), by applying it consistently to each quantile of the POT-GPD distribution. Then, GPD parameters are re-estimated based on the corrected exceedance sample.

For $u > \tilde{u}_t$, the annual exceedance rate of wind speed can be expressed as:

$$\Lambda(x, y, u) = \lambda_{U>u_t}(x, y)\left[1 + \tilde{k}_U(x, y)\frac{u - \tilde{u}_t(x, y)}{\tilde{\sigma}_U(x, y)}\right]^{-1/\tilde{k}_U(x,y)} \qquad (8)$$

where $\tilde{u}_t$, $\tilde{\sigma}_U$ and $\tilde{k}_U$ are re-estimated GPD parameters, and the term in brackets represents the Generalized Pareto survival function. This continuous probabilistic representation enables evaluation of wind hazard at any intensity level, rather than at selected return periods, and allows convolution with structural fragility curves according to Eq. (1).

2.2. Structure vulnerability

The adopted vulnerability model is grounded on literature-based fragility curves. In the following, the wording ‘vulnerability’ is adopted to describe how susceptible a system, structure, or asset is to damage or failure when exposed to hazard, while the wording ‘fragility’ represents the quantitative probabilistic expression of vulnerability. Fragility curves describe the probability of loading demand D exceeding structural capacity C under given values x of im. By assuming that both C and D follow a log-normal distribution because of the central limit theorem [48], the fragility curve follows in turn a log-normal distribution described by

$$P_F = P[D \geq C | im = x] = \Phi\left(\frac{\ln x - \mu_F}{\sigma_F}\right), \qquad (9)$$

being Φ the CDF of the standard normal distribution of mean value μ_F and standard deviation σ_F of $\ln x$. Investigations of wind fragility curves

Table 1
Fragility curves examined in the literature: geometrical parameters of the lattice towers (height H, span L, base width B) and adopted modelling approach.

Authors	H [m]	L [m]	B [m]	Modelling approach
Fu and Li [53]	99.9	500	n.a.	IDA
Cai et al. [19]	62.5	150,275,400	8.67	SM
Fu et al. [36]	43.5	n.a.	8.32	MSA
Tian et al. [49]	102	1118	25	IDA
Xue et al. [20]	31.5	200	3	MSA
Xue et al. [54]	31.5	n.a.	3	SM
Ma et al. [55]	25.25	300	3.51	MSA
Wang et al. [50]	44	100,200,300,400,500	8.56	MSA
Bi et al. [56]	87.3	400	14.69	MSA
Dikshit and Alipour [57]	43.9	n.a.	n.a.	MSA
Zhu et al. [58]	92	100	17.28	IDA
Zhang et al. [59]	34	n.a.	4.96	SM
Zhu et al. [51]	103.3	200	9.8	SR
Feng and Stewart [60]	44	200	11	SM

for structures deployed along line-like infrastructure have focused on several key assets, including lattice towers (e.g. [19]), long-span suspension bridges (e.g. [27]), traffic signal structures (e.g. [28]), trees (e.g. [32]), among others. In the following, the focus is placed on lattice towers along transmission lines.

State-of-the-art approaches to assess wind fragility curves of lattice towers can be classified in the following categories: *incremental dynamic analysis* (IDA, e.g. [49]), *multi-stripe analysis* (MSA, e.g. [50]), *surrogate models* (SM, e.g. [19]), *structural robustness* based methods (SR, e.g. [51]), *uncertainty analysis* based methods (e.g. [52]). Regardless of the adopted approach, according to Fu et al. [36], the fragility curve of a given lattice tower can be accurately estimated by modelling three adjacent towers and four adjacent conductors (three-tower four-conductor system). Lattice towers do not behave as isolated structures under wind loading. Instead, their response and failure modes are influenced by the forces transmitted through the conductors. As such, the three-tower four-conductor system is recognized as a sound compromise between full mechanical fidelity and computational cost. Alternatively, simplified models that consider a single tower with two conductors, where the influence of adjacent towers is simulated through ad hoc boundary conditions, have also been proposed [36]. The full list of examined studies is shown in Table 1, along with the considered lattice tower height H, conductor span length L, tower base width B, and the modelling approach adopted by the Authors.

As an illustrative example, Fig. 3(a) collects fitted log-normal fragility curves from the studies listed in Table 1, for a fixed wind direction orthogonal to the alignment and for different L. The discrepancy among them is striking, even for a fixed value of L. It is worth stressing that, for a given class of problem (e.g. lattice towers subjected to wind hazard), fragility curves are not universal while they depend on: (i) the deterministic parameters of the considered structural system, embodied by the lattice tower topology, dimensions (H, B, L), but also the nominal value of each parameter affecting its capacity; (ii) the considered aleatory uncertainties ascribable to different sources of vulnerability; (iii) the model uncertainty arising from the different modelling approaches to define the fragility curve; (iv) the chosen im.

The choice and characterization of different vulnerability sources is not uniform among studies in the literature. Most studies implement aleatory uncertainties ascribable to *mechanical vulnerability* source, embodied by the random material mechanical properties, structural member cross-sections, geometric imperfections, among others. *Aerodynamic and aeroelastic vulnerabilities* conversely are seldomly considered and embody the aerodynamic coefficients the structure and structural properties affecting aeroelastic loads. Some noteworthy examples include the random characterization of the drag coefficient of lattice tower system [50] or bridge aeroelastic properties [27]. Finally, some studies also consider *wind exposure vulnerability* by introducing uncertain incoming wind flow conditions. Wang et al. [50] consider a random exponent in the power low describing the mean wind speed profile, while Banday et al. [27] introduces uncertain wind turbulence characteristics into the evaluation of the fragility curve.

Concerning model uncertainty, uncertainty in fragility assessment may arise from structural modelling [61]. In particular, Ma et al. [55] show how component-based and global fragility analysis may give rise to sensibly different results. Furthermore, not all the examined studies specify how many Monte Carlo realizations are performed and if statistical convergence is achieved.

Concerning the definition of im, even if the majority of the analysed studies adopts the reference wind speed U measured at 10 m from the ground, the averaging time is not uniform (e.g. 10-minute [50], 1-minute [55]) or not specified, while others adopt the gust wind speed [60].

Within this framework, μ_F should mainly reflect variations of deterministic input parameters, while σ_F should reflect the uncertainty propagation arising from random input parameters. A preliminary attempt to investigate how the main geometrical properties of the structural system affect μ_F is carried out, under the oversimplified assumption that lattice towers behave like cantilever beams subjected to an horizontal pulling force at their top induced by the suspended conductors, and an horizontal uniform distributed load induced by wind. Assuming this, the resistant couple at the base of the tower is proportional to $M_0 \propto qH^2/2 + HwL^2/8s$, being q the distributed horizontal wind load along the tower, w the distributed weight along the cables, and s the sag. As a result, the resistant axial force acting on the members at the base of the tower is proportional to $N_0 \propto M_0/B \propto H(H + L^2/s)/B$. Finally, since s is seldomly reported among the examined studies, it is set proportional to L. Therefore, the relation above is simplified to $N_0 \propto H(H + L)/B$. Fig. 3(b) shows the scatter plot of N_0-μ_F for the examined studies in Table 1. Specifically, μ_F is globally inversely proportional to $H(H+L)/B$, showing that, under the same value of B, transmission towers of higher height or with longer conductor spans are generally more fragile to wind. However, variability among considered studies is not negligible and should be mainly referred to variations of other nominal parameters like lattice tower topology, cross-section dimensions, material mechanical properties, among others.

Fig. 3(c) shows how uncertainty propagates from input random variables to the resulting fragility curve in terms of coefficient of variation $c.o.v.$ In particular, input random variables are grouped into material (Poisson ratio ν, Young's modulus E, yield strength f_y), geometrical (member thickness t, member width b), load (wind speed coefficients c_U, drag coefficient C_D) and structural (structural damping ξ, joints yield strength V_y) uncertainties. The $c.o.v.$ of the fragility F is represented in terms of boxplot, in order to describe its overall variability. Fig. 3(c) confirms how there is no general agreement about the amount of random parameters to be considered and the value of $c.o.v.$ associated to reach random variable. Furthermore, it shows how the $c.o.v.$ is nor sensibly dumped nor sensibly amplified within fragility analysis.

2.3. Exposure

The exposure can be mapped in digital format over large domains thanks to Geographic Information System (GIS) and related datasets describing both the infrastructure and the structures deployed along it. Examples of global datasets of critical infrastructures vulnerable to wind hazard include, among others, overhead power lines and the lattice towers along them (e.g. [62]), highways and the bridges or traffic panels along them (e.g. [63]), railways and the multiple technical components along them, e.g. stations, electric line poles, or turnouts (e.g. [64]). As an illustrative example, Fig. 4 shows the complete Italian and Swiss overhead power networks, distinguishing between medium voltage (<220 kV), high voltage (220 kV, 380 kV) and extra-high voltage (>380 kV) lines.

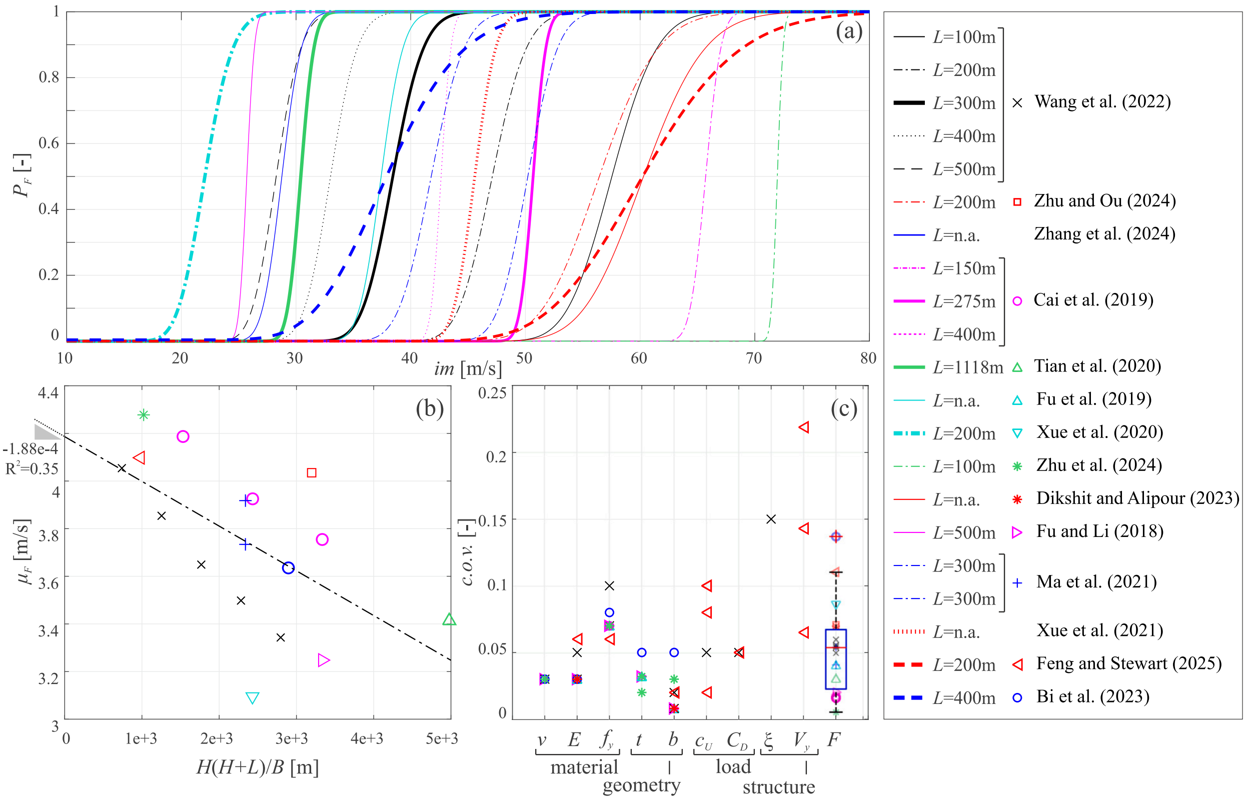

Fig. 3. Comparison among fitted log-normal fragility curves of lattice towers collected from the literature (a). Deterministic variability among fragility curves: μ_F as a function of $H(H+L)/B$ (b). Random variability among fragility curves: comparison between coefficient of variations of input variables and resulting fragility F (c).

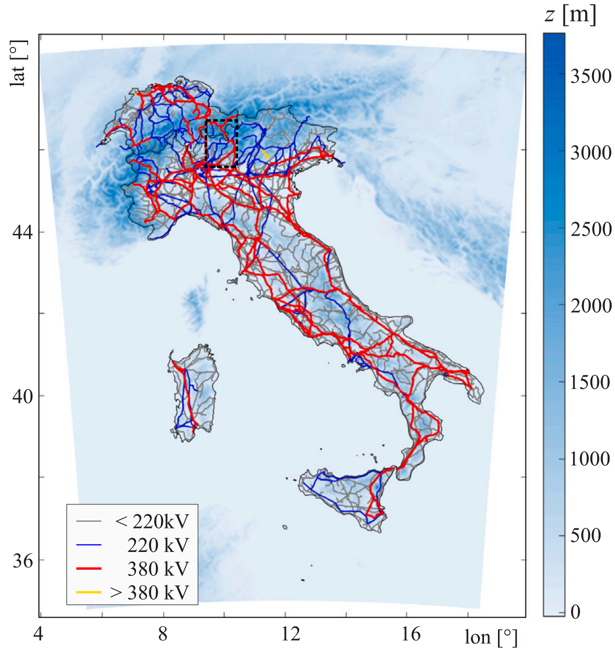

Fig. 4. Italian and Swiss overhead power networks from OpenInfraMap [62] database based on OpenStreetMap.

In this study, the exposure $E(x, y)$ is simply set as a logical index that identifies the geographical location of the infrastructure. No specific lines or network segments are assigned weights based on the potential consequences of their failure. Economic and social losses can be calculated by multiplying the annual probability of failure by e.g. repair costs, outage duration, population served [16].

3. Application setup

In the following, the hazard, vulnerability and exposure determinants are discussed by referring to the specific application considered in this study.

In Fig. 5, the performance of the wind hazard model is critically discussed by referring to wind impact on lattice towers. During the night between 28–29 October 2018, four lattice towers located in the Albula pass (CHE, Fig. 5a) collapsed because of the destructive Vaia storm [65]. The close-up view in Fig. 5(b) depicts the orography in the surrounding of the collapsed towers through isocontour lines, distinguishing between the Engadin Valley and the Albula pass. Overlaid are wind speed magnitudes and vectors derived from the VHR dataset at 04:00 on 29 October 2018, i.e. approximately the time of the collapse, with horizontal resolution equal to the VHR grid spacing. Wind speeds are noticeably higher over regions of elevated orography and are predominantly aligned from west-northwest to east-southeast. In contrast, a significant reduction in wind intensity is observed within the Engadin Valley, owing to its sheltering effect, which also induces deviations in wind direction along the valley axis.

Measured wind speed in correspondence of the Albula pass is not available [66]. As a result, Fig. 5(c) compares VHR data from the closest VHR cell (see highlighted cell in red in Fig. 5b) with closest compliant stations in terms of mesoscale representativeness (i.e. anemometric stations expected to not be sensibly affected by microscale effects due to uniform orography and roughness in their neighbourhood [11]) and ERA5 data from the closest ERA5 cell (see highlighted cell in magenta

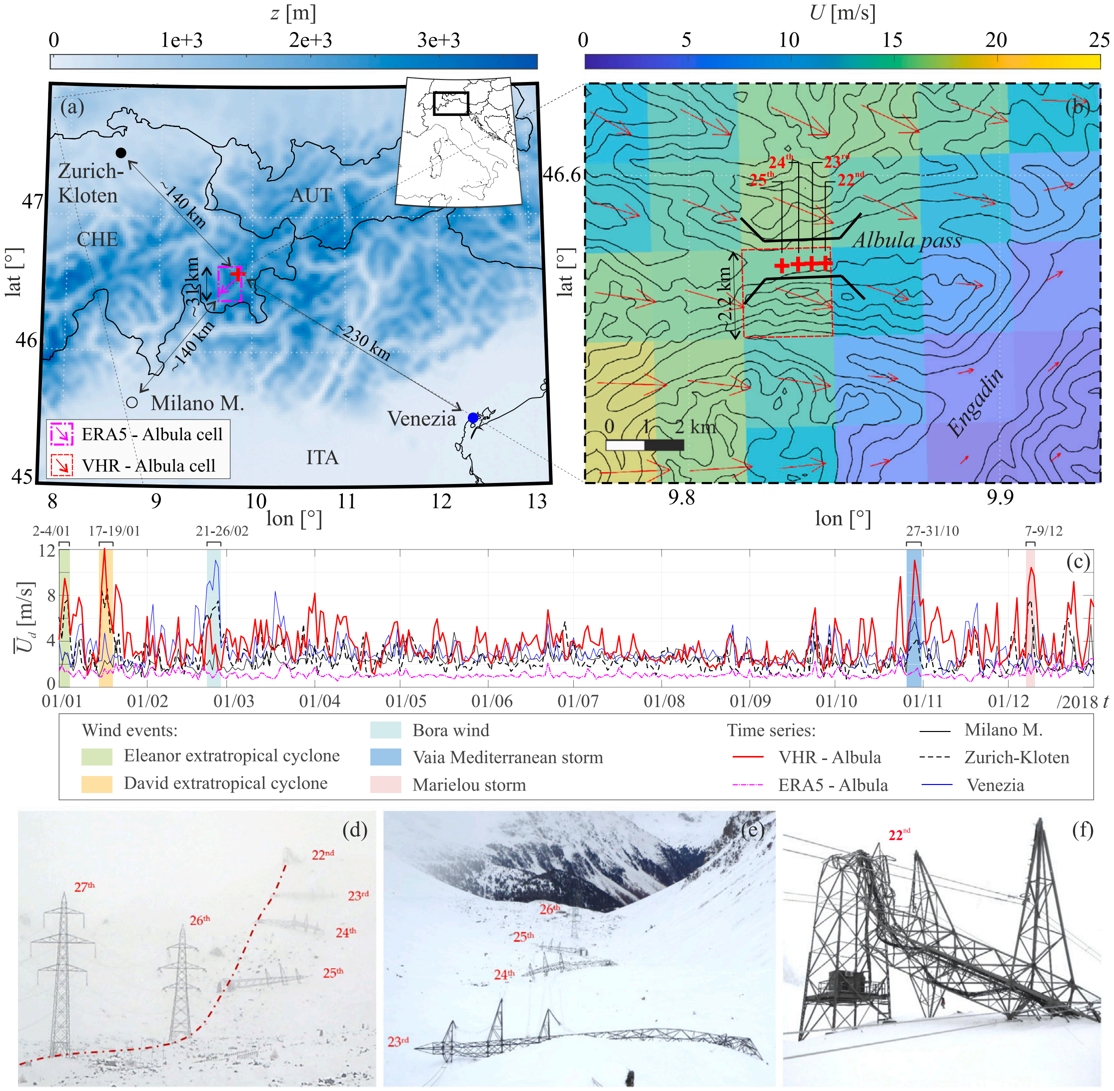

Fig. 5. Location of Zurich-Kloten, Milano Malpensa, and Venezia airport anemometric stations in relation to the location of lattice towers collapsed during storm Vaia with superimposed wind direction from ERA5 dataset at 04:00 on 29 October 2018 (a). Close-up view of the Albula pass showing the orography with superimposed wind speed magnitude and direction from VHR dataset at 04:00 on 29 October 2018 (b). Time series of daily average wind speed $\overline{U}_d$ during the year 2018 (c) from mesoscale representative stations VHR-Albula. Pictures taken in the aftermath of the event (d–f, after [66,67]). (For interpretation of the references to colour in this figure legend, the reader is referred to the web version of this article.)

in Fig. 5a). In particular, the time series from the airport stations of Zurich-Kloten, Milano Malpensa, and Venezia (marked in Fig. 5a), and the VHR-Albula cell containing the location of collapsed towers (see highlighted cell in Fig. 5b) are compared during the whole year 2018 in terms of daily average wind speed $\overline{U}_d$. From a qualitative perspective, the wind speed data grounding the wind hazard model confirms its capability in simulating mesoscale phenomena since individual mesoscale events are clearly recognized along the time series. Elanor and Friederike storms occurred in January are clearly captured by VHR-Albula and Zurich-Kloten station since Eleanor mainly travelled from UK to Switzerland and southern France, while Friederike mainly crossed Netherland and Germany [68]. The strong Bora wind event occurred in February in northeastern Italy [69] is primarily captured by Venice station. The destructive Vaia Mediterranean storm occurred in late October [70] is clearly visible on each time series even with different intensities. Finally, Marielou storm occurring in December [71] mainly affected southeastern France, resulting into being mainly captured by VHR-Albula, Zurich-Kloten and Malpensa stations. From a quantitative perspective, wind speed intensities increase markedly from measured to REA-based VHR-Albula wind speed, primarily due to the strong orographic effects exerted by mountain slopes at the meso-γ scale.

The impact of downscaling from ERA5 to VHR is striking both in terms of wind speed intensity (Fig. 5c) and directionality (see vector directions in Fig. 5a,b). The ERA5-Albula wind speeds are systematically lower than the corresponding VHR estimates, reflecting the smoothing of orographic forcing associated with the coarser ERA5 horizontal resolution. Moreover, the instantaneous wind direction in ERA5 differs substantially from those obtained from VHR, as the coarse ERA5 grid cannot adequately resolve the uneven orography. However, it is important to note that the wind speeds derived from VHR-Albula are not fully representative of the local microscale conditions experienced by the collapsed towers since orographic variation occurring within the VHR cell extent are not directly modelled (see the highlighted cell crossing the Albula pass in Fig. 5b). The 2.2 km horizontal resolution of the hazard model captures mesoscale wind features relevant for regional-scale risk mapping while microscale effects occurring at spatial scales smaller than the grid resolution, such as channelling, speed-up induced by slopes, uneven micro-terrain sector-based wind exposure induced by roughness, are not explicitly resolved. Accordingly, the

Table 2
Uncertain input parameters considered in [50] for the assessment of fragility curves.

Category	Component	Description	Parameter	*c.o.v.*	PDF
Geometry	Tower	Member thickness	t	0.032	Normal
		Member width	b	0.008	Normal
		Member imperfection	I_m	–	Uniform
		Global imperfection	I_g	–	Uniform
	Cables	Diameter	d	0.02	Normal
Material	Tower	Elastic modulus	E_t	0.03	Log-normal
		Poisson ratio	ν	0.03	Log-normal
		Yield strength	$f_{y,t}$	0.07	Log-normal
	Cables	Elastic modulus	E_c	0.05	Normal
		Tensile strength	$f_{y,c}$	0.1	Normal
	Insulator	Elastic modulus	E_i	0.02	Normal
		Tensile strength	$f_{y,i}$	0.05	Normal
Dynamics	Tower	Damping ratio	ξ	0.15	Log-normal
Aerodynamics	Tower	Drag coefficient	$C_{D,t}$	0.05	Truncated normal
	Cables	Drag coefficient	$C_{D,c}$	0.05	Truncated normal
Mean wind speed	–	Power law exponent	e	0.05	Truncated normal

proposed framework is intended for infrastructure mesoscale risk assessment, and to eventually plan microscale risk assessment studies to refine the mesoscale risk analysis to the scale of the individual lattice tower by accounting for localized changes in orography. If detailed local assessment studies are required, the framework can be coupled with microscale downscaling approaches, such as computational wind engineering simulations or wind tunnel testing (e.g. [72]).

The pictures showing the aftermath of the extreme event are shown in Fig. 5(d–f). The four towers collapsed in the direction orthogonal to the line, without causing the rupture of the conductor. In particular, the 22nd is the only lattice tower that failed at mid-eight, while the remaining three failed at the base. Fig. 5(e) shows the steep lateral slope of the Albula pass, responsible of a microscale wind channelling effect along its axis.

Lattice towers vulnerability is modelled by adopting the fragility curves assessed by Wang et al. [50] because of (i) the largest amount of modelled conductor span lengths among the considered studies, i.e. L = {100, 200, 300, 400, 500} m; (ii) the broad number of input uncertain parameters related to structural, aerodynamic, and wind exposure vulnerability sources; and (iii) the setting of the reference 10-minute average wind speed measured at 10 m from the ground as *im*, in agreement with European standards for wind load assessment [73]. Given the omnidirectional wind hazard model, vulnerability is quantified through the most unfavourable fragility curve provided in [50], i.e. the one resulting by setting wind direction orthogonal to the alignment.

It is worth stressing that the adopted fragility curves were not calibrated or validated against the specific lattice tower configurations deployed along the considered transmission corridor. Furthermore, no distinction is made between tangent and angle towers. All lattice towers are assumed to share the same fragility model, with dependence of vulnerability captured primarily through differences in conductor span length. This assumption reflects in the scope of the study, which aims at defining a comprehensive modelling framework rather than assessing asset-specific reliability, and it is motivated by the lack of comprehensive fragility datasets that characterize tangent and angle tower typologies under wind loading assuming span length variability. The modelling framework allows the adoption of detailed, corridor-specific fragility curves, whenever available.

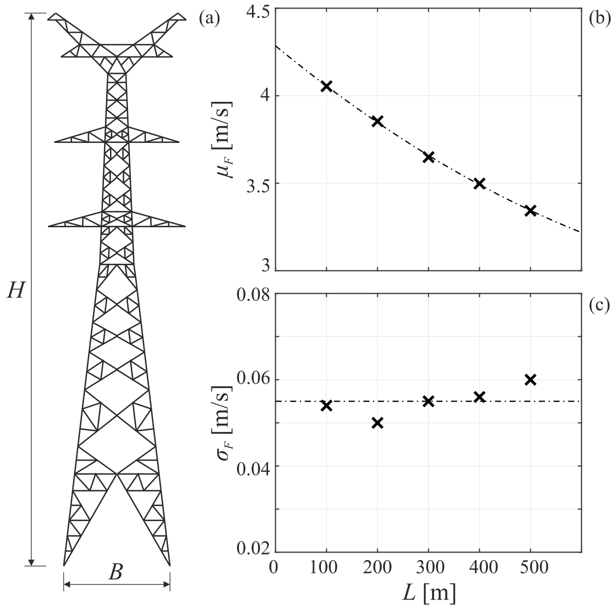

Fig. 6. Geometry of the lattice tower referring to the adopted fragility curves (a, redrawn from [50]), their mean values μ_F (b) and standard deviation σ_F (c) fitted versus the cable span L.

In the following, the procedure followed by Wang et al. [50] to assess fragility curves is briefly recalled, as well as the input uncertain parameters considered in their analysis. The tower's fragility curves were obtained through Nonlinear Dynamic Analysis on a three-tower four-conductor system. The eigenmode assembly method and displacement updating method are adopted to account for both local member and global imperfections. Uncertain input parameters set in [50] are listed in Table 2 by reporting their coefficient of variation *c.o.v.* and PDF type. In the table, they are grouped into 5 categories, referring to mechanics (geometry, material, dynamics), aerodynamics, and wind exposure (mean wind speed) to highlight distinct vulnerability sources. To assess the tower's fragility curve, (i) 30 FE models of the imperfect tower-line system are generated incorporating mechanical vulnerability sources; (ii) 30 sets of mean wind speed time series are simulated for the tower-line system incorporating wind exposure vulnerability source; (iii) Nonlinear Dynamic Analysis is performed for each pair of structural model and set of wind speed time series incorporating aerodynamic vulnerability source.

The transmission tower overall geometry is depicted in Fig. 6(a), together with the resulting trends of μ_F (b) and σ_F (c) over L. $\mu_F(L)$ and $\sigma_F(L)$ are interpolated through a decreasing quadratic law and a constant value, respectively.

The exposure is set by considering the transnational transmission corridor spanning between Sils (Sils im Domleschg, CHE) and Gorlago (Bergamo, ITA) substations. Its geographical location and the definition of the curvilinear coordinate s are shown in Fig. 7(a). Sils (s = 0 km) and Gorlago (s = 192.5 km) are connected through 5 in-series transmission lines connecting the intermediate substations Filisur (s = 18.7 km), La Punt (s = 43.5 km), Robbia (s = 74.1 km) and San Fiorano (s = 130.7 km). Fig. 7(b) shows the altitude profile z traversed by the lines, highlighting the three mountain passes crossed by the lines, i.e. Albula, Bernina, and Mortirolo, while Fig. 7(c) plots the conductor span length L associated with each lattice tower along the line. It appears evident that L reduces in correspondence of mountain passes, reflecting design adaptations aimed at reducing the vulnerability of lattice towers in poorly accessible areas where strong winds generally expected. Furthermore, a general increase on L is observed

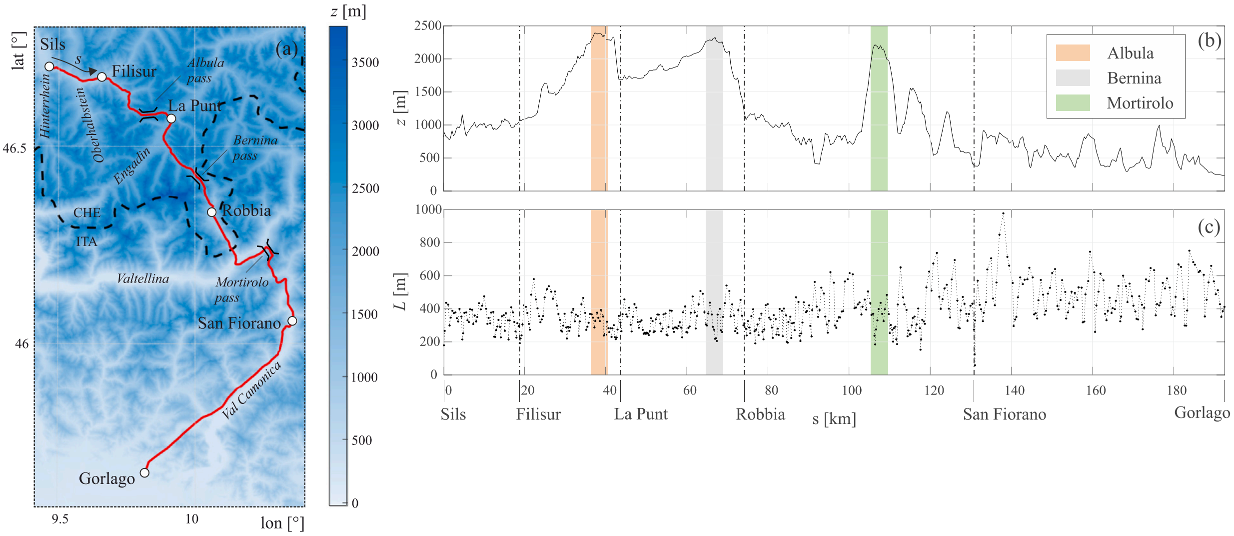

Fig. 7. Sils-Gorlago transmission corridor: geographical map highlighting substations, mountain passes and valleys (a), along-line altitude profile z (b) and conductor span length L (c).

when moving from Switzerland towards Italy, probably due to different transmission line design habits.

4. Results

In the following, multiple resulting risk maps are presented and critically discussed. They differ in their dimensionality, extent of the covered domain, and design perspectives:

- (trans)national two-dimensional (2D) risk map to assist during the planning of extension or maintenance of wide infrastructure network(s) (Section 4.1);
- line-like one-dimensional (1D) risk map to assist during the design and/or relocation of transmission line(s) (Section 4.2);
- point-like 0-dimensional (0D) risk map to assist during the design and/or performance assessment of lattice tower(s) (Section 4.3).

Risk is calculated by numerically solving Eqs. (1)–(3). The computational cost scales with the cardinality of hazard realizations per cell #, and the number of query cells n_c. For the considered application, risk assessment was completed within 98, 2.8, and 1.1 hr on a standard workstation, respectively for the 2D (# = 1e+6, n_c = 4.44e+6), 1D (# = 1e+7, n_c = 1.3e+3) and 0D (# = 1e+7, n_c = 5.1e+2) maps. It is worth stressing that, due to the lack of a fragility model validated against the specific lattice towers deployed along the considered transmission corridor, results are interpreted in a comparative perspective, rather than as asset-specific failure probabilities.

4.1. 2D risk map for infrastructure networks

Transnational 2D risk maps can be drafted to assist during the planning and maintenance of infrastructure networks deployed over wide territories. In the following, the exposure index is set uniform and equal to $E = 1$ over the whole Italian and Swiss lands to highlight how hazard and risk maps are related.

Fig. 8 shows the Italian and Swiss national wind hazard maps U_{50} for a 50-year return period (a), risk maps P_f considering uniform $L = 400$ m all over the whole national territories (b), sample hazard curves (c), and scatter plots showing the correlation between hazard and risk in terms of dimensionless indices (d,e). The spatial distribution of P_f follows qualitatively the pattern of U_{50} (Fig. 8a,b). P_f results higher in correspondence of areas where U_{50} is high, e.g. mountainous areas like Alps and the Apennine ridge, and lower in correspondence of areas where U_{50} is low, e.g. flat plains sheltered by mountain ridges like the Po valley in northern Italy and the Swiss Plateau. However, U_{50} and P_f do not exhibit a linear correlation, as illustrated in Fig. 8(d) through their corresponding dimensionless indices I_H and I_R. Indices are defined in order to normalize hazard and risk metrics in the range $[0, 1]$ so to make them directly comparable, i.e. $I_H = \frac{U_{50}-\min(U_{50})}{\max(U_{50})-\min(U_{50})}$ and $I_R = \frac{P_f-\min(P_f)}{\max(P_f)-\min(P_f)}$. Although the wind load demand scales with the square of U, the relationship between I_H and I_R exhibits a much higher-order dependence. The fitting of the scatter plot with the power law $I_R = I_H^{\alpha}$ returns $\alpha = 5$ with high coefficient of determination $R^2 = 0.88$ and high Spearman's correlation coefficient $\rho_s = 0.9$. On the one hand, the relationship between I_H and I_R reflects the nonlinearity introduced by the fragility curve, accounting for sources of uncertainty inherent in both demand and capacity, embodied by the slope of the fragility curve, i.e. σ_F. On the other hand, U_{50} (i.e. I_H) does not describe alone the full hazard curve Λ (see Eq. (2)). According to Cito and Iervolino [74], and in analogy to the seismic engineering risk assessment framework, the slope of the linear approximation of the hazard curve is another key parameter for risk assessment. To this aim, Fig. 8(c) plots two exemplificatory hazard curves showing similar U_{50} and sensibly different slopes k of the hazard curve in the neighbourhood of U_{50}, with $k = \frac{\Lambda^+(u=U_{50})-\Lambda^-(u=U_{50})}{U_{50}^+-U_{50}^-}$, being φ^- and φ^+ the right and left neighbourhood of the variable φ. In particular, the higher k, the more frequent wind occurrences with $U > U_{50}$. Fig. 8(e) shows the scatter plot between the normalized slope $k^* = \frac{k-\min(k)}{\max(k)-\min(k)}$ and I_R. The scatter does not depict a marked trend as in Fig. 8(d). However, geographical locations exhibiting high values of k^* are more commonly associated with higher wind-induced risk, showing a moderate correlation $\rho_s = 0.49$.

Within this perspective, the 2D map of I_H may be adopted, together with k^*, for preliminary identification of the wind impact by adopting an index-based quantitative approach [75].

4.2. 1D risk map of transmission lines

Within a risk-informed design framework, the proposed methodology effectively supports the design process and/or relocation of existing transmission lines by providing quantitative performance metrics, enabling designers and decision-makers to rank and select alternative solutions.

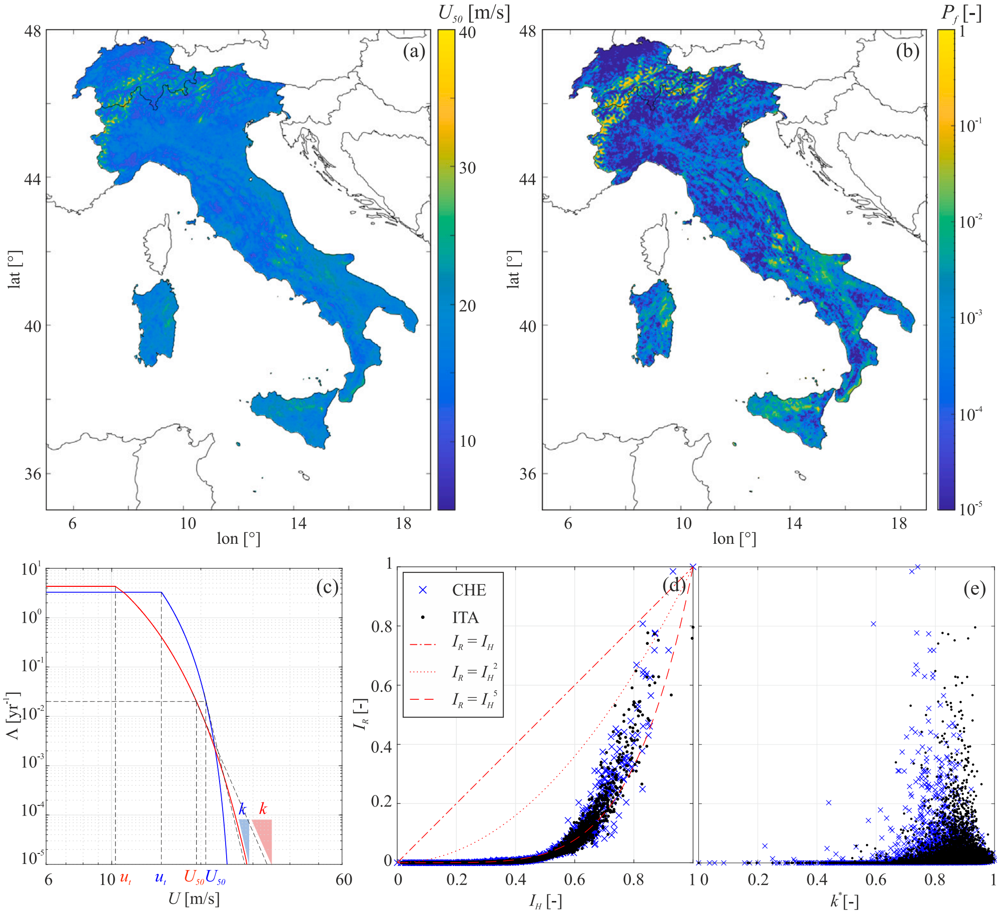

Fig. 8. Italian and Swiss national maps of wind hazard U_{50} (a), and wind-induced risk P_f (b) for $L = 400$ m and uniform exposure $E = 1$. Sample hazard curves and related U_{50} and slope k (c), correlation scatter-plots between hazard I_H and risk I_R indices (d), normalized slope k^* and risk index I_R (e).

As a benchmark case study, two alternative power transmission alignments connecting the villages of Tiefencastel and Celerina (CHE) are analysed. The first alignment, corresponding to the existing line (s_1), crosses the Albula valley and Albula pass before descending into the Engadin valley. The hypothetical second alignment (s_2) follows the Sursette valley starting from Tiefencastel, where an existing transmission corridor is already present, and subsequently enters the Engadin valley through Septimer pass to finally reach Celerina. The two alternative alignments are georeferenced in Fig. 9(c).

The along-line hazard U_{50} and the corresponding failure probability of the tower P_f for uniform along-line L values are plotted in Fig. 9(a,b) for s_1 and s_2, respectively. $U_{50}(s)$ is obtained by sampling the local hazard values from the spatial tiles intersected by each alignment, thereby implicitly capturing the influence of roughness and topography at the mesoscale along the route. For the existing alignment s_1, U_{50} exhibits a pronounced increase along the route, with a particularly steep rise near the Albula pass, where extreme wind speeds locally exceed 20 m/s. This reflects the typical speed-up induced by mountain slopes. The alternative alignment s_2 exhibits overall higher U_{50} values throughout its length. Specifically, U_{50} (i) gradually increases along the Sursette valley, which ascends southwards; (ii) reaches its maximum value (again exceeding 20 m/s) in correspondence of the Septimer pass; and (iii) subsequently decreases upon entering the Engadin valley, where the shielding effect of the valley reduces extreme winds.

The corresponding risk P_f qualitatively follows the trend of U_{50}. P_f reaches its maximum at the mountain passes, consistent with the highest along-line wind hazard (see Fig. 9c, for $L = 200$ m). Moreover, P_f systematically increases with L, reflecting the shift of the fragility curve towards low *im* (Fig. 6b) and the fact that longer spans are inherently more fragile under the same hazard conditions.

Finally, Fig. 9(d) shows the potential range of the line probability of failure through its upper ($\hat{P}_{f,line}$) and lower ($\check{P}_{f,line}$) bounds. For $L = 200$ m, the overall probability of failure of the alternative alignment s_2 is notably lower than that of s_1, consistent with the along-line P_f shown in Fig. 9(c). However, as the span length increases to $L = 300$ m, the two probabilities exhibit comparable ranges, and for $L = 400$ m, the riskiest alignment shifts from s_1 to s_2. This shift can be attributed to two main factors: (i) the slightly higher extreme wind speeds along the Sursette valley compared to those in the Albula valley, which primarily amplify $\check{P}_{f,line}$; and (ii) the greater total length of s_2, which results in a larger number of towers and consequently increases the cumulative risk $\hat{P}_{f,line}$. It should also be noted that $[\check{P}_{f,line}, \hat{P}_{f,line}]$ encompasses more than one order of magnitude, preventing the precise estimation of the actual line probability of failure. Nevertheless, within comparative risk assessment frameworks, the upper and lower bounds remain useful for identifying the most risk-prone alignment.

The analysis above intentionally isolates the wind-related hazard and risk components, thereby neglecting other critical aspects that should be incorporated into a holistic design framework for transmission line infrastructures. In practical applications, decisions regarding route selection are influenced not only by wind hazard conditions but also by broader economic and strategic considerations. These may include, for example, the construction and maintenance costs associated with alternative alignments, environmental and land-use constraints, accessibility and constructability issues, and the risk assessment of the alignment when embedded within a countrywide power transmission network.

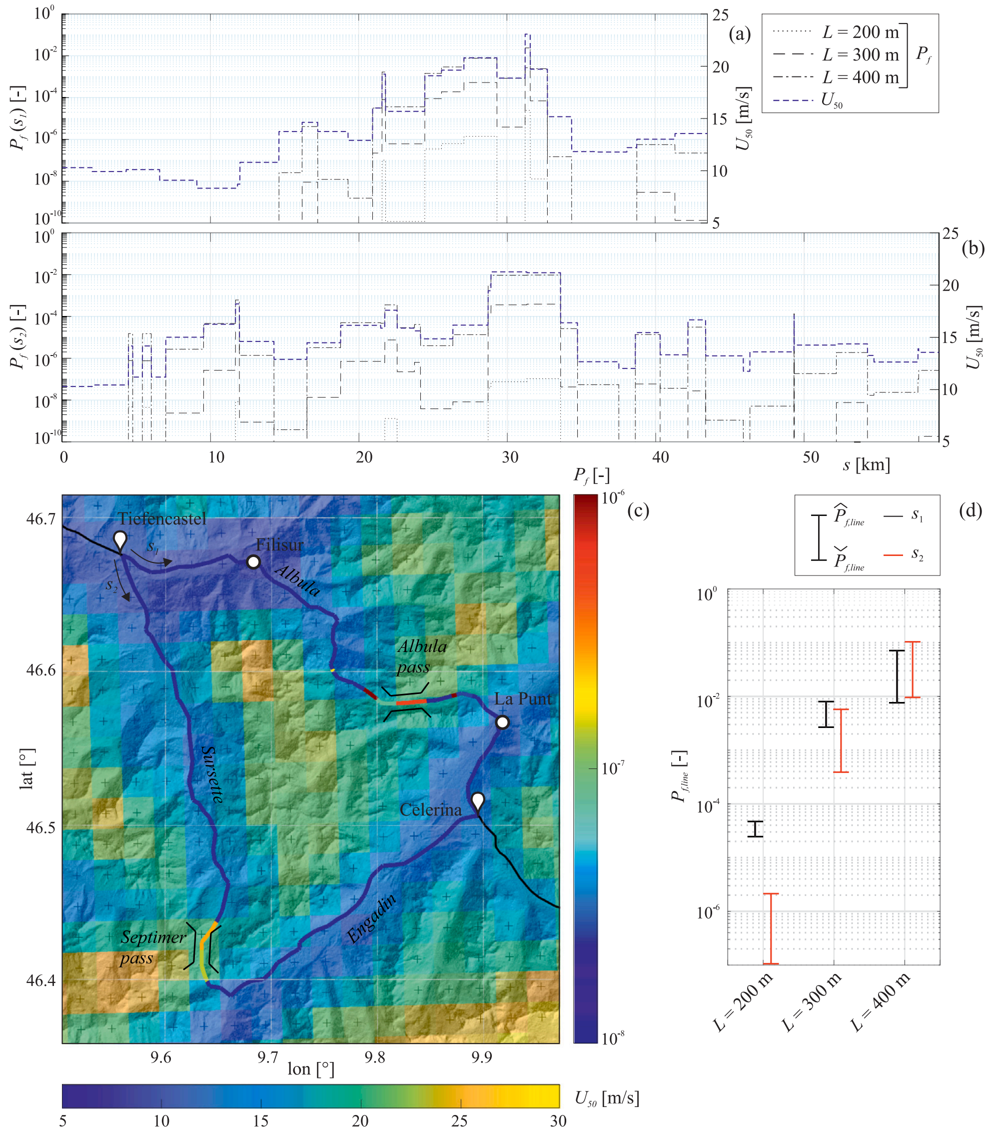

Fig. 9. Comparison between two alternative alignments between Tiefencastel and Celerina. Along-line P_f and U_{50} (a,b), georeferenced layout assuming a constant span length $L = 200$ m (c), and resulting lower and upper bounds of the line probability of failure $P_{f,line}$ (d).

4.3. 0D risk map of lattice towers

Finally, the proposed framework can be adopted to assist during the design and/or performance assessment of point-like lattice towers along transmission lines.

The along-line risk assessment of the lattice towers is quantified along the transnational power transmission corridor georeferenced in Fig. 7(a) by considering the actual conductor span length L suspended by each tower, in agreement with Fig. 7(c). Fig. 10(a) shows the along-line variation of both U_{50} and the pointwise P_f in correspondence of individual lattice towers. The same quantities are georeferenced in Fig. 10(b) where it becomes evident that the strongest wind extremes are typically associated with regions of steep orography, whereas valleys generally experience lower wind intensities. Notably, high values of P_f occur in correspondence with the Albula and Bernina passes, where the wind hazard exhibits a pronounced increase due to orographic effects. In contrast, the Mortirolo pass shows relatively lower P_f values, consistent with the lower U_{50}. Interestingly, a local rise of P_f is also observed near the San Fiorano substation, despite the absence of particularly high U_{50} values. This local increase of failure probability is attributed to the increase in span length L. Detailed close-up views of the Albula and Bernina passes, as well as the San Fiorano substation, are provided in Fig. 10(c–e). These panels highlight how P_f is jointly amplified by hazard, here represented through U_{50}, and vulnerability, here driven by the span length L. The combined spatial variability of hazard and fragility underlines the importance of along-line 0D risk mapping to identify the most critical lattice towers to prioritize inspection and maintenance interventions or to plan microscale risk assessment studies.

It is worth noting that the highest values of P_f are not obtained in correspondence of the Albula pass, despite past collapses of lattice towers reported in this area [66]. Conversely, the highest P_f are attained near the Bernina pass, where no tower failures have been documented to date. According to the Author, this apparent inconsistency arises from several factors. First, wind hazard has been evaluated at the mesoscale, and therefore, local microscale effects are not captured by the present hazard model. Although the adopted hazard model provides an unprecedented very high spatial resolution of about 2 km, it is still insufficient to accurately represent microscale wind flow channelling effects occurring within the narrow Albula Pass. Secondly, the fragility functions employed in this study do not correspond to the specific lattice towers currently installed along the Sils-Gorlago

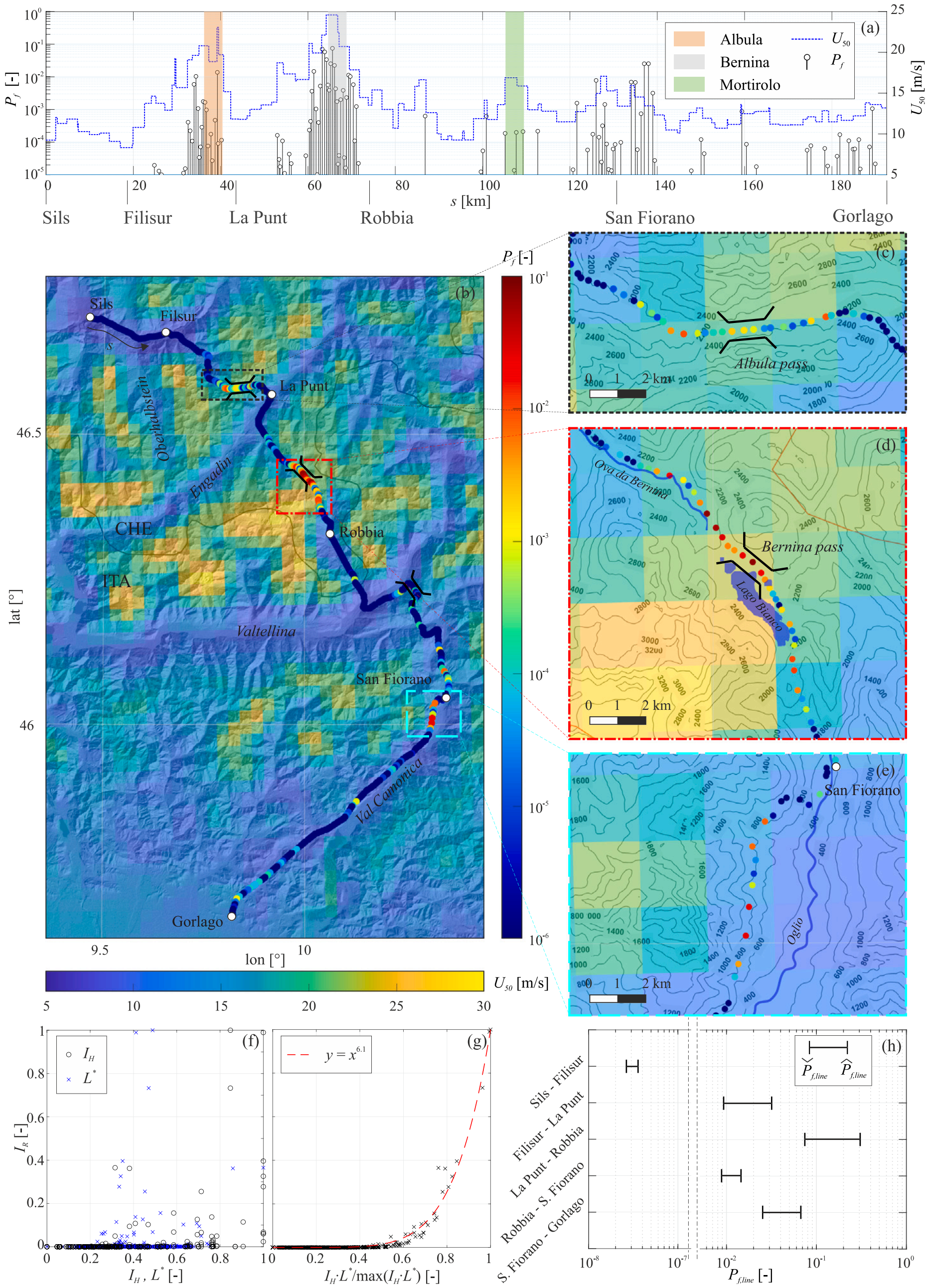

Fig. 10. Along-line P_f and U_{50} (a). Georeferenced layout (b) with close-up views around Albula pass (c), Bernina pass (d), San Fiorano substation (e). Correlation scatter-plots between hazard index I_H, dimensionless span L^* and risk index I_R (f,g). Resulting line probabilities of failure $P_{f,line}$ (e).

transmission corridor. Thirdly, the actual towers in service are likely to have been designed to withstand the locally severe wind environment, thus exhibiting higher capacity in wind-prone regions.

The correlation between hazard index I_H and risk index I_R is shown in Fig. 10(f). When compared with the correlation obtained at the Italian and Swiss national scales (Fig. 8d), the along-line correlation is significantly lower, yielding a Spearman's correlation coefficient $\rho_s = 0.65$. Such a low correlation can be primarily attributed to the spatial variability of the span length L along the transmission corridor. Towers suspending longer spans tend to exhibit higher P_f, thereby introducing additional dispersion in I_R. The correlation between the normalized span length $L^* = \frac{L-\min(L)}{\max(L)-\min(L)}$ and I_R is shown in the same figure, resulting in a correlation coefficient of similar magnitude, i.e. $\rho_s = 0.49$. Since I_R scales proportionally to both I_H and L^*, Fig. 10(g) depicts the scatter plot of their normalized product. The resulting scatter plot displays a markedly stronger monotonic correlation, with $\rho_s = 0.93$, well described by a power law trend exhibiting a coefficient of determination $R^2 = 0.98$. This confirms the use of such indicators as efficient means for preliminary risk assessment of lattice towers.

Finally, the overall probability of failure of each line segment, $P_{f,line}$, is illustrated in Fig. 10(g), where both lower and upper bounds are reported. The resulting ranges of $P_{f,line}$ reflect the combined effect of the entity of individual tower risks P_f and the length of each corresponding line segment. It is particularly noteworthy that the San Fiorano-Gorlago line segment exhibits a higher overall probability of failure than the Filisur-La Punt section. This outcome can be primarily attributed to the generally larger span lengths L adopted in Italy relative to those adopted in Switzerland (see Fig. 7b), and the long distance covered by the line segment compared with the others.

5. Conclusions

This study contributes to bridging the long-standing gap between seismic and wind risk mapping by developing and testing a novel, high-resolution wind risk assessment framework.

The approach is demonstrated by focusing on lattice towers deployed along transmission lines as infrastructure class, and on a transnational corridor between Italy and Switzerland as specific application. This case study is chosen due to the critical nature of such a class of infrastructure, the known vulnerability of lattice towers to wind action, and the particularly challenging benchmark provided by the uneven orography and surface roughness across the Alpine region. Wind hazard is grounded on the high resolution reanalysis-based approach for the assessment of the mesoscale design wind speed recently introduced by Raffaele et al. [11]. The resulting mesoscale hazard maps reach seismic hazard ones in terms of spatial resolution, spatial covering and homogeneity. Fragility curves are obtained from the literature. A critical review of state-of-the-art fragility models for lattice towers is carried out to investigate their sensitivity to both deterministic and uncertain input parameters. Exposure is set as a logical index that identifies the geographical location of the infrastructure. The resulting failure probability of lattice towers allows to infer the lower and upper bounds of the failure probability of the transmission line.

The results of the proposed methodological framework are organized and discussed through maps with differ dimensionality, extent of the covered domain, and addressed to distinct design perspectives. Transnational 2D risk mapping assists designers during both the planning of extension or maintenance of wide infrastructure networks. Line-like 1D risk mapping along alternative alignments assists the design and the potential relocation of transmission lines. Point-like 0D along-line risk mapping of lattice towers along a specific transnational transmission corridor proves effective for evaluating the risk of individual structures within a network. Overall, results demonstrate the potential of the proposed methodological framework to support decision-making processes within the planning, design and maintenance of critical infrastructures thanks to the enhancement of the wind hazard link within the PBWE chain. Nevertheless, the present study should be regarded as one component of a broader multi-criteria decision-making framework. Furthermore, although the adopted resolution allows unprecedented mesoscale hazard and risk mapping, it may require the coupling of localized downscaling approaches where significant microscale effects are expected.

In light of the obtained results, several research needs arise. First, future studies could aim at developing a simplified analytical framework for wind risk assessment in analogy to the well-established Cornell's methodology in seismic risk analysis [48]. Secondly, obtained results indicate that the estimated range of probability of line failure may encompass more than one order of magnitude. This highlights the need for statistical modelling approaches that explicitly account for the cross and spatial correlation of the intensity measures along line-like infrastructure systems, in analogy with probabilistic seismic hazard analysis for spatially distributed systems [37]. Thirdly, the proposed modelling framework could be tested against georeferenced historical data about failures of lattice towers, and adapted for future climate scenarios by exploiting climate projections [41] instead of reanalysis. Finally, this study highlights the strong variability of lattice towers' fragility curves induced by aleatory and model uncertainties. Accordingly, future work should statistically quantify these uncertainties, examine the statistical convergence of the fragility curve parameters, and assess how uncertainty in input parameters propagate to the fragility curves. Such efforts would strengthen one of the weakest links in the PBWE chain by enabling the robust definition of wind fragility curves for different structural types.

Declaration of competing interest

The authors declare that they have no known competing financial interests or personal relationships that could have appeared to influence the work reported in this paper.

Acknowledgements

This study was developed in the framework of the research project PROtection Technologies from Eolian Events for Coastal Territories (PROTEECT, http://www.proteect.polito.it/) within the Ministerial Decree no. 1062/2021 and received funding from the FSE REACT-EU - PON Ricerca e Innovazione 2014–2020. This manuscript reflects only the Author's views and opinions, neither the European Union nor the European Commission can be considered responsible for them. This study was jointly carried out within the RETURN Extended Partnership and received funding from the European Union Next-GenerationEU (National Recovery and Resilience Plan – NRRP, Mission 4, Component 2, Investment 1.3 – D.D. 1243 2/8/2022, PE0000005) – SPOKE TS 2. The Author thanks L. Bruno, member of the GeoWindy R&D group (https://geowindy.polito.it) at the Department of Architecture and Design - Politecnico di Torino, for the stimulating discussions about the topic of the study.

Data availability

Data will be made available on request.

References

[1] Poljanšek K, Bono F, Gutiérrez E. Seismic risk assessment of interdependent critical infrastructure systems: the case of european gas and electricity networks. Earthq Eng Struct Dyn 2012;41(1):61–79. http://dx.doi.org/10.1002/eqe.1118.

[2] Braik AM, Ma X, Koliou M, Kaihatu JM, Pinell S. Assessing hurricane risks in coastal communities: A participatory and probabilistic approach incorporating evolving hazard conditions. Eng Struct 2026;346:121684. http://dx.doi.org/10.1016/j.engstruct.2025.121684.

[3] Ciampoli M, Petrini F, Augusti G. Performance-Based Wind Engineering: Towards a general procedure. Struct Saf 2011;33(6):367–78. http://dx.doi.org/10.1016/j.strusafe.2011.07.001.

[4] Porter KA. An overview of PEER's performance-based earthquake engineering methodology. In: Proceedings of ninth international conference on applications of statistics and probability in civil engineering, Vol. 52, 2003, p. 3729–35.

[5] Isyumov N, Alan G. Davenport's mark on wind engineering. J Wind Eng Ind Aerodyn 2012;104–106:12–24. http://dx.doi.org/10.1016/j.jweia.2012.02.007.

[6] Picozzi V, Landi F, Avossa A, Croce P, Formichi P, Ricciardelli F. The climatic action uncertainty chain. Eng Struct 2024;301:117357. http://dx.doi.org/10.1016/j.engstruct.2023.117357.

[7] Ballio G, Lagomarsino S, Piccardo G, Solari G. Probabilistic analysis of italian extreme winds: Reference velocity and return criterion. Wind Struct 1999;2(1):51–68. http://dx.doi.org/10.12989/was.1999.2.1.051.

[8] Ricciardelli F, Akbaba A, Picozzi V, Avossa A. An updated wind hazard map of Italy. J Build Eng 2025;115:114457. http://dx.doi.org/10.1016/j.jobe.2025.114457.

[9] Technical standards for construction - update dm January 17, 2018. Standard, Rome, Italy: Ministry of Infrastructures and Transport; 2018.

[10] Guide for the assessment of wind actions and effects on structures. Standard, Rome, Italy: National Research Council (CNR); 2018.

[11] Raffaele L, Bruno L, Colucci E. Reanalysis-based mesoscale wind maps for the design of structures and infrastructures with an application to Italy. J Wind Eng Ind Aerodyn 2024;253:105844. http://dx.doi.org/10.1016/j.jweia.2024.105844.

[12] Lupoi G, Franchin P, Lupoi A, Pinto PE. Seismic fragility analysis of structural systems. J Eng Mech 2006;132(4):385–95. http://dx.doi.org/10.1061/(ASCE)0733-9399(2006)132:4(385).

[13] Smith A, Lott N, Vose R. The integrated surface database: Recent developments and partnerships. Bull Am Meteorol Soc 2011;92(6):704–8. http://dx.doi.org/10.1175/2011BAMS3015.1.

[14] Meletti C, Marzocchi W, D'amico V, Lanzano G, Luzi L, Martinelli F, Pace B, Rovida A, Taroni M, Visini F, et al. The new Italian seismic hazard model (MPS19). Ann Geophys 2021;64(1). http://dx.doi.org/10.4401/ag-8579.

[15] Herbin A, Barbato M. Fragility curves for building envelope components subject to windborne debris impact. J Wind Eng Ind Aerodyn 2012;107:285–98. http://dx.doi.org/10.1016/j.jweia.2012.05.005.

[16] Crowley H, Colombi M, Borzi B, Faravelli M, Onida M, Lopez M, Polli D, Meroni F, Pinho R. A comparison of seismic risk maps for italy. Bull Earthq Eng 2009;7(1):149–80. http://dx.doi.org/10.1007/s10518-008-9100-7.

[17] Masi A, Lagomarsino S, Dolce M, Manfredi V, Ottonelli D. Towards the updated italian seismic risk assessment: exposure and vulnerability modelling. Bull Earthq Eng 2021;19(8):3253–86. http://dx.doi.org/10.1007/s10518-021-01065-5.

[18] Hallowell ST, Myers AT, Arwade SR, Pang W, Rawal P, Hines EM, Hajjar JF, Qiao C, Valamanesh V, Wei K, et al. Hurricane risk assessment of offshore wind turbines. Renew Energy 2018;125:234–49. http://dx.doi.org/10.1016/j.renene.2018.02.090.

[19] Cai Y, Xie Q, Xue S, Hu L, Kareem A. Fragility modelling framework for transmission line towers under winds. Eng Struct 2019;191:686–97. http://dx.doi.org/10.1016/j.engstruct.2019.04.096.

[20] Xue J, Mohammadi F, Li X, Sahraei-Ardakani M, Ou G, Pu Z. Impact of transmission tower-line interaction to the bulk power system during hurricane. Reliab Eng Syst Saf 2020;203:107079. http://dx.doi.org/10.1016/j.ress.2020.107079.

[21] Ma L, Christou V, Bocchini P. Framework for probabilistic simulation of power transmission network performance under hurricanes. Reliab Eng Syst Saf 2022;217:108072. http://dx.doi.org/10.1016/j.ress.2021.108072.

[22] Greco SF, Dikshit S, Stankovski A, Gjorgiev B, Alipour A, Sansavini G. Operational risk assessment of electric power grids exposed to straight-line winds. Reliab Eng Syst Saf 2025;266:111709. http://dx.doi.org/10.1016/j.ress.2025.111709.

[23] Raffa M, Reder A, Marras GF, Mancini M, Scipione G, Santini M, Mercogliano P. VHR-REA_IT Dataset: Very High Resolution Dynamical Downscaling of ERA5 Reanalysis over Italy by COSMO-CLM. Data 2021;6(8). http://dx.doi.org/10.3390/data6080088.

[24] Mara T, Hong H. Effect of wind direction on the response and capacity surface of a transmission tower. Eng Struct 2013;57:493–501. http://dx.doi.org/10.1016/j.engstruct.2013.10.004.

[25] de Souza RR, Miguel LFF, Lopez RH, Miguel LFF, Torii AJ. A procedure for the size, shape and topology optimization of transmission line tower structures. Eng Struct 2016;111:162–84. http://dx.doi.org/10.1016/j.engstruct.2015.12.030.

[26] Bilionis DV, Vlachakis K, Vamvatsikos D, Dasiou M-E, Vayas I, Lagouvardos K. Risk assessment of rehabilitation strategies for steel lattice telecommunication towers of greece under extreme wind hazard. Eng Struct 2022;267:114625. http://dx.doi.org/10.1016/j.engstruct.2022.114625.

[27] Banday ZZ, Fenerci A, Nord TS, Øiseth OA. Fragility analysis of long-span bridges under wind hazard. J Wind Eng Ind Aerodyn 2025;267:106252. http://dx.doi.org/10.1016/j.jweia.2025.106252.

[28] Wieghaus KT, Mander JB, Hurlebaus S. Fragility analysis of wind-excited traffic signal structures. Eng Struct 2015;101:652–61. http://dx.doi.org/10.1016/j.engstruct.2015.07.044.

[29] Meng X, Tian L, Liu J, Jin Q, Yang F. Wind-ice-induced damage risk analysis for overhead transmission lines considering regional climate characteristics. Eng Struct 2025;329:119844. http://dx.doi.org/10.1016/j.engstruct.2025.119844.

[30] Meng X, Tian L, Liu J, Jin Q. Failure prediction of overhead transmission lines incorporating time series prediction model for wind-ice loads. Reliab Eng Syst Saf 2025;259:110927. http://dx.doi.org/10.1016/j.ress.2025.110927.

[31] Raffaele L, Bruno L. Windblown sand action on civil structures: Definition and probabilistic modelling. Eng Struct 2019;178:88–101. http://dx.doi.org/10.1016/j.engstruct.2018.10.017.

[32] Gardiner B, Lorenz R, Hanewinkel M, Schmitz B, Bott F, Szymczak S, Frick A, Ulbrich U. Predicting the risk of tree fall onto railway lines. Forest Ecol Manag 2024;553:121614. http://dx.doi.org/10.1016/j.foreco.2023.121614.

[33] Freda A, Solari G. A pilot study of the wind speed along the rome-naples HS/HC railway line, part 2-probabilistic analyses and methodology assessment. J Wind Eng Ind Aerodyn 2010;98(8–9):404–16. http://dx.doi.org/10.1016/j.jweia.2009.12.005.

[34] Dolce M, Prota A, Borzi B, da Porto F, Lagomarsino S, Magenes G, Moroni C, Penna A, Polese M, Speranza E, et al. Seismic risk assessment of residential buildings in italy. Bull Earthq Eng 2021;19(8):2999–3032. http://dx.doi.org/10.1007/s10518-020-01009-5.

[35] Ebeling CE. An introduction to reliability and maintainability engineering. Waveland Press; 2019.

[36] Fu X, Li H-N, Tian L, Wang J, Cheng H. Fragility analysis of transmission line subjected to wind loading. J Perform Constr Facil 2019;33(4):04019044. http://dx.doi.org/10.1061/(ASCE)CF.1943-5509.0001311.

[37] Poudel A, Pitilakis K, Silva V, Rao A. Infrastructure seismic risk assessment: an overview and integration to contemporary open tool towards global usage. Bull Earthq Eng 2023;21(9):4237–62. http://dx.doi.org/10.1007/s10518-023-01693-z.

[38] Hersbach H, Bell B, Berrisford P, Hirahara S, Horányi A, Sabater J Muñoz, Nicolas J, Peubey C, Radu R, Schepers D, Simmons A, Soci C, Abdalla S, Abellan X, Balsamo G, Bechtold P, Biavati G, Bidlot J, Bonavita M, Chiara G De, Dahlgren P, Dee D, Diamantakis M, Dragani R, Flemming J, Forbes R, Fuentes M, Geer A, Haimberger L, Healy S, Hogan RJ, Hólm E, Janisková M, Keeley S, Laloyaux P, Lopez P, Lupu C, Radnoti G, de Rosnay P, Rozum I, Vamborg F, Villaume S, Thépaut J-N. The ERA5 global reanalysis. Q J R Meteorol Soc 2020;146(730):1999–2049. http://dx.doi.org/10.1002/qj.3803.

[39] Orlanski I. A rational subdivision of scales for atmospheric processes. Bull Am Meteorol Soc 1975;56(5):527–30.

[40] Yang S, Chouinard LE, Langlois S. Hourly wind data for aeolian vibration analysis of overhead transmission line conductors. J Wind Eng Ind Aerodyn 2022;230:105184. http://dx.doi.org/10.1016/j.jweia.2022.105184.

[41] Raffa M, Adinolfi M, Reder A, Marras GF, Mancini M, Scipione G, Santini M, Mercogliano P. Very High Resolution Projections over Italy under different CMIP5 IPCC scenarios. Sci Data 2023;10:238. http://dx.doi.org/10.1038/s41597-023-02144-9.

[42] Torrielli A, Repetto MP, Solari G. Extreme wind speeds from long-term synthetic records. J Wind Eng Ind Aerodyn 2013;115:22–38. http://dx.doi.org/10.1016/j.jweia.2012.12.008.

[43] Outten S, Sobolowski S. Extreme wind projections over Europe from the Euro-CORDEX regional climate models. Weather Clim Extrem 2021;33:100363. http://dx.doi.org/10.1016/j.wace.2021.100363.

[44] Coles S. An introduction to statistical modeling of extreme values. In: Springer series in statistics, London: Springer-Verlag; 2001.

[45] Effects on structures. Standard, Zurich, Switzerland: Swiss engineer and Architects association; 2020.

[46] Vozila A Belušić, Belušić D, Prtenjak M Telišman, Güttler I, Bastin S, Brisson E, Demory M-E, Dobler A, Feldmann H, Hodnebrog Ø, Kartsios S, Keuler K, Lorenz T, Milovac J, Pichelli E, Raffa M, Soares PMM, Tölle MH, Truhetz H, de Vries H, Warrach-Sagi K. Evaluation of the near-surface wind field over the Adriatic region: local wind characteristics in the convection-permitting model ensemble. Clim Dyn 2023;61:4319–42. http://dx.doi.org/10.1007/s00382-023-06703-z.

[47] Piccolroaz S, Amadori M, Toffolon M, Dijkstra HA. Importance of planetary rotation for ventilation processes in deep elongated lakes: Evidence from Lake Garda (Italy). Sci Rep 2019;9(8290). http://dx.doi.org/10.1038/s41598-019-44730-1.

[48] Cornell CA, Jalayer F, Hamburger RO, Foutch DA. Probabilistic basis for 2000 sac federal emergency management agency steel moment frame guidelines. J Struct Eng 2002;128(4):526–33. http://dx.doi.org/10.1061/(ASCE)0733-9445(2002)128:4(526).

[49] Tian L, Zhang X, Fu X. Fragility analysis of a long-span transmission tower–line system under wind loads. Adv Struct Eng 2020;23(10):2110–20. http://dx.doi.org/10.1177/1369433220903983.

[50] Wang J, Li H-N, Fu X, Dong Z-Q, Sun Z-G. Wind fragility assessment and sensitivity analysis for a transmission tower-line system. J Wind Eng Ind Aerodyn 2022;231:105233, URL 10.1016/j.jweia.2022.105233.

[51] Zhu X, Ou G. Wind fragility modeling of transmission tower-line system based on threat-dependent structural robustness index. Struct Saf 2025;114:102571. http://dx.doi.org/10.1016/j.strusafe.2024.102571.

[52] Fu X, Du W-L, Li G, Dong Z-Q, Li H-N. A data-driven method for the reliability analysis of a transmission line under wind loads. Steel Compos Struct 2024;52(4):461–73. http://dx.doi.org/10.12989/scs.2024.52.4.461.

[53] Fu X, Li H-N. Uncertainty analysis of the strength capacity and failure path for a transmission tower under a wind load. J Wind Eng Ind Aerodyn 2018;173:147–55. http://dx.doi.org/10.1016/j.jweia.2017.12.009.

[54] Xue J, Xiang Z, Ou G. Predicting single freestanding transmission tower time history response during complex wind input through a convolutional neural network based surrogate model. Eng Struct 2021;233:111859. http://dx.doi.org/10.1016/j.engstruct.2021.111859.

[55] Ma L, Khazaali M, Bocchini P. Component-based fragility analysis of transmission towers subjected to hurricane wind load. Eng Struct 2021;242:112586. http://dx.doi.org/10.1016/j.engstruct.2021.112586.

[56] Bi W, Tian L, Li C, Ma Z, Pan H. Wind-induced failure analysis of a transmission tower-line system with long-term measured data and orientation effect. Reliab Eng Syst Saf 2023;229:108875. http://dx.doi.org/10.1016/j.ress.2022.108875.

[57] Dikshit S, Alipour A. A moment-matching method for fragility analysis of transmission towers under straight line winds. Reliab Eng Syst Saf 2023;236:109241. http://dx.doi.org/10.1016/j.ress.2023.109241.

[58] Zhu C, Yang Q, Huang G, Zhang X, Wang D. Fragility analysis and wind directionality-based failure probability evaluation of transmission tower under strong winds. J Wind Eng Ind Aerodyn 2024;246:105668. http://dx.doi.org/10.1016/j.jweia.2024.105668.

[59] Zhang W-S, Fu X, Li H-N, Zhu D-J. Wind-induced fragility analysis of a transmission tower based on multi-source monitoring data and deep learning methods. J Wind Eng Ind Aerodyn 2024;252:105834. http://dx.doi.org/10.1016/j.jweia.2024.105834.

[60] Feng Y, Stewart MG. Probabilistic analysis of wind-induced failures of transmission tower-line systems. Struct Infrastruct Eng 2025;1–14. http://dx.doi.org/10.1080/15732479.2025.2554724.

[61] Iervolino I. Assessing uncertainty in estimation of seismic response for PBEE. Earthq Eng Struct Dyn 2017;46(10):1711–23. http://dx.doi.org/10.1002/eqe.2883.

[62] Open infrastructure map. 2025, URL https://openinframap.org/.

[63] Global roads open access data set, version 1. In: Center for international earth science information network-CIESIN-columbia university and information technology outreach services-ITOS-university of Georgia. Palisades, NY: NASA Socioeconomic Data and Applications Center (SEDAC); 2025, URL https://doi.org/10.7927/H4X63JTX.

[64] Open railway map. 2023, URL https://www.openrailwaymap.org/.

[65] Swissgrid. Windstorm vaia causes damage in the transmission grid. 2018, URL https://www.swissgrid.ch/en/home/newsroom/newsfeed/20181030-01.html.

[66] Vettoretto G. (Ph.D. thesis), Politecnico di Milano; 2020, URL https://hdl.handle.net/10589/185906.

[67] Vettoretto G, Li Z, Affolter C. Evaluation of the ultimate collapse load of a high-voltage transmission tower under excessive wind loads. Buildings 2023;13(2):513. http://dx.doi.org/10.3390/buildings13020513.

[68] Vautard R, van Oldenborgh GJ, Otto FEL, Yiou P, de Vries H, van Meijgaard E, Stepek A, Soubeyroux J-M, Philip S, Kew SF, Costella C, Singh R, Tebaldi C. Human influence on european winter wind storms such as those of january 2018. Earth Syst Dyn 2019;10(2):271–86. http://dx.doi.org/10.5194/esd-10-271-2019.

[69] Nimbus Web. Fine Febbraio-inizio Marzo 2018: gelo intenso e tardivo, neve a Roma, Napoli e Bari. 2018, (in Italian) URL http://www.nimbus.it/eventi/2018/180302GeloItalia.htm.

[70] Cavaleri L, Bajo M, Barbariol F, Bastianini M, Benetazzo A, Bertotti L, Chiggiato J, Davolio S, Ferrarin C, Magnusson L, Papa A, Pezzutto P, Pomaro A, Umgiesser G. The october 29, 2018 storm in Northern Italy - an exceptional event and its modeling. Prog Oceanogr 2019;178:102178. http://dx.doi.org/10.1016/j.pocean.2019.102178.

[71] World Meteorological Organization. Annual bulletin on the climate in WMO region VI. 2018, URL https://www.dwd.de/DE/leistungen/ravibulletinjahr/archiv/bulletin_2018.pdf?__blob=publicationFile&v=1.

[72] Bao X, Lou W, Gu Y, Liao S, Lu Z, Cai W. Judgment criteria for significant wind speed-up regions in natural complex terrain. J Wind Eng Ind Aerodyn 2024;249:105724. http://dx.doi.org/10.1016/j.jweia.2024.105724.

[73] Eurocode 1 – actions on structures – part 1- 4: general actions – wind actions. Standard, Brussels, Belgium: European Committee for Standardization (CEN); 2005, p. 1–4.

[74] Cito P, Iervolino I. Drivers to seismic hazard curve slope. Earthq Eng Struct Dyn 2024;53(15):4497–510. http://dx.doi.org/10.1002/eqe.4226.

[75] Gliksman D, Averbeck P, Becker N, Gardiner B, Goldberg V, Grieger J, Handorf D, Haustein K, Karwat A, Knutzen F, et al. A european perspective on wind and storm damage–from the meteorological background to index-based approaches to assess impacts. Nat Hazards Earth Syst Sci 2023;23(6):2171–201. http://dx.doi.org/10.5194/nhess-23-2171-2023.